ACS APPLIED NANO MATERIALS

www.acsanm.org Article

In-Gap States of HfO_2 Nanoislands Driven by Crystal Nucleation: Implications for Resistive Random-Access Memory Devices

Niclas Schmidt, Konstantin Z. Rushchanskii,* Urška Trstenjak, Regina Dittmann, and Silvia Karthäuser*

Cite This: *ACS Appl. Nano Mater.* 2023, 6, 148−159 Read Online

ACCESS | Metrics & More | Article Recommendations | Supporting Information

ABSTRACT: Envisioned extremely scaled, high-performance memory devices request to conduct the step from thin semiconductor films to nanoscale structures and the use of promising high-*k* materials such as hafnium oxide (HfO_2). HfO_2 is well suited for use in resistive random-access memory (ReRAM) devices based on the valence change mechanism. Here, we provide a decidedly scaled system, namely, HfO_2 nanoislands that are grown by van der Waals epitaxy on highly oriented pyrolytic graphite (HOPG). The electronic and structural properties of these well-separated, crystalline HfO_2 nanoislands are investigated by scanning probe methods as well as ab initio methods. The topography reveals homogeneously formed HfO_2 nanoislands with areas down to 7 nm^2 and a thickness of one unit cell. They exhibit several acceptor- and donor-like in-gap states in addition to the bulk band gap, implying bulk properties. X-ray photoelectron spectroscopy indicates hafnium carbide formation as one possible origin for defect states. Going further to the crystal nucleation of HfO_2, nanocrystals with a diameter of 2.7−4.5 Å are identified next to carbon vacancies in the topmost HOPG layer, indicating that carbon is incorporated into the islands at early nucleation stages. A precise description of these nuclei is accomplished by the simulation of small Hf_mO_n(:C) clusters (m = 3 to 10; n = 3 to 22) with and without carbon incorporation using ab initio methods. The comparison of the theoretically determined lowest-energy clusters and electronic states with the experimental results allows us to identify the structure of the most relevant HfO_2 sub-nanometer crystals formed during the first nucleation steps and the nature of the in-gap states found at the surfaces of HfO_2 nanoislands. That way, a model system is derived that consists of distinct structural units, related to surface states or defect states, respectively, that will promote the tailoring of in-gap states of smallest HfO_2 structures and thus the scalability of memory devices.

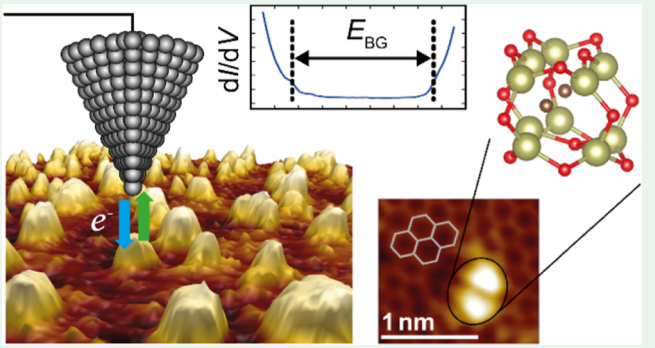

KEYWORDS: *HfO_2 nanoislands, scalability, carbon incorporation, in-gap states, crystal nucleation*

1. INTRODUCTION

HfO_2 is a material that has gained substantial attention owing to its memristive and ferroelectric properties, as well as its already achieved integration with Si-based complementary metal-oxide-semiconductor (CMOS) technology.[1−5] HfO_2-based thin films exhibit unconventional ferroelectricity, robust down to sub-10 nm dimensions, and enhanced polar distortions have been observed in the ultrathin regime.[3] The spontaneous polarization is generally attributed to the metastable polar orthorhombic phase ($Pca2_1$). Different approaches have been utilized to stabilize this polar phase, such as particle size reduction, implementation of dopants or oxygen vacancies, and the application of epitaxial strain.[6,7]

Resistive random-access memory (ReRAM) devices based on HfO_2 show great promise for next-generation non-volatile memories owing to their potential for high speed, low power consumption, and ultimate scalability. HfO_2 ReRAM devices belong to the valence change mechanism (VCM) type, which is based on the resistive hysteresis driven by oxygen vacancy drift and the resulting redox reactions.[8,9] The formation of oxygen vacancies is affected by the crystallinity of the film, as well as by doping of HfO_2 with other transition metal ions.[10] Different resistive switching properties are observed in amorphous and polycrystalline films where grain boundaries can serve as conductive pathways, owing to the high density of oxygen vacancies at these locations.[11] It is essential for the improvement of nanosized hafnia-based ReRAM devices to understand in detail the nature of surface and defect states which are located at the surface of HfO_2-based thin films and grain boundaries, leading to the distinctly enhanced conductivity.[12] Here, we aim to get an understanding at the atomic

Received: September 20, 2022
Accepted: October 3, 2022
Published: October 24, 2022

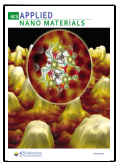

scale on how the growth conditions of HfO_2 nanocrystals (NCs) can guide the formation of in-gap states that are of relevance for the later performance of resistive switching memory devices.

HfO_2-based thin films have been grown by various techniques, such as atomic layer deposition (ALD),[13,14] molecular beam epitaxy (MBE),[8,15] and pulsed laser deposition (PLD).[16] The recently developed van der Waals growth method enables thin film or island growth without epitaxial strain and formation of defects and thus the study of intrinsic thin film or island properties.[17,18] The main challenge for realizing oxide growth on highly oriented pyrolytic graphite (HOPG) using this method is the inherent incompatibility of the two groups of materials. In order to obtain crystalline oxides with a stoichiometric composition, the growth of oxide thin films or islands usually is carried out at high temperatures and in oxidizing conditions, where the chemical stability of HOPG is low.[19] This may induce the formation of hafnium carbide (HfC), like observed recently,[20] despite the need for temperatures of 1600−2000 °C for a carbothermic reduction otherwise.[21] Here, we perform a careful adaption of the growth conditions to ensure the growth of low-defect thin HfO_2 films, while the damage to the HOPG surface is kept low.

With regard to the scalability of memory devices, the step from closed thin films to nanoislands of a few unit cells shows great potential. A powerful tool for the investigation of semiconductor band gaps at the nanoscale is scanning tunneling spectroscopy (STS).[22,23] So far, it has been shown with STS that the band gap of semiconductor materials decreases when lowering the thickness from a few monolayers to a single monolayer.[24] Furthermore, STS allows us to detect electronic states close to or within the band gap, which can be caused by defects or surface states and thus has a huge potential for the characterization of smallest semiconductor nanostructures down to NCs.[25,26]

In this study, we investigate the intrinsic properties of HfO_2 nanoislands grown on HOPG by van der Waals epitaxy via PLD. In order to provide the best possible conditions for defect-free nanoislands, instead of using high-vacuum conditions, the growth is carried out in an inert gas atmosphere, which reduces the kinetic energy of the plasma-plume particles. The topography of the HfO_2 nanoislands and, moreover, the crystal nucleation of HfO_2 is studied using scanning tunneling microscopy (STM) at the atomic scale. Furthermore, we examine the electronic structure of the nanoislands with a special focus on the band gap and in-gap states with the local precision offered by STS and supplemented by X-ray photoelectron spectroscopy (XPS). Additionally, the performed ab initio calculations of the structure and the electronic states of a series of small Hf_mO_n(:C) clusters with or without carbon incorporation allow us to reveal the role of carbon in crystal nucleation and to identify the nature of characteristic in-gap states.

2. EXPERIMENTAL SECTION

2.1. Pulsed Laser Deposition. HOPG substrates mounted onto custom-made holders were freshly cleaved using adhesive tape and directly inserted into the PLD vacuum chamber (Surface Systems and Technology GmbH & Co. KG, Germany) with a base pressure of 10^{-8} mbar. Heating of the substrates to a deposition temperature of 650 °C was performed with a backside laser heater. A KrF excimer laser (λ_{laser} = 248 nm) with a repetition rate of 4 Hz was used to ablate a polycrystalline HfO_2 target (SurfaceNet GmbH, Germany) with a laser fluence of 2.0 J cm^{-2} for the duration of the growth of 5 s. The HfO_2 islands were deposited in an inert gas atmosphere, p(Ar) = 0.065 mbar, with a target-to-substrate distance of 51 mm. The samples were quenched to room temperature immediately after deposition and reached temperatures below 400 °C already after 90 s. [For further details, see Supporting Information, Chapter (I), Figures S1−S3.].

2.2. STM and STS Analyses. STM and STS were carried out using a commercial low-temperature (LT) ultrahigh vacuum scanning tunneling microscope (CreaTec Fischer & Co. GmbH, Germany) operating at T = 5 K and a base pressure below 10^{-10} mbar. Electrochemically etched tungsten tips were used in STM and STS measurements and cleaned prior to use by high-voltage pulses. Tip artefacts were ruled out by testing the tip on a Au(111) substrate first, featuring well-defined atomic steps (STM) and Shockley-type surface states (STS). Tip modifications during measurement were excluded by comparison of STS spectra on pristine HOPG and bare HOPG between HfO_2 nanoislands (see Figure S4). Topography images were taken in constant-current mode. Differential conductance measurements were performed using standard lock-in techniques with the tip grounded and the feedback loop switched-off. The tip-sample separation (TSS) was defined by the applied voltage and current set points, V_{set} and I_{set}, respectively. All STM images were processed with SPIP 6.7.4 software (Image Metrology A/S, Denmark), and common filter methods were deployed.

2.3. XPS Analysis. XPS was conducted with a Versa Probe 5000 (Physical Electronics, Inc., USA) with monochromatic X-rays generated by an Al K-alpha source and an excitation energy of 1486.6 eV. The detection angle of all spectra shown in this work was set to 45°. The spectra were evaluated by CasaXPS V2.3.18 (Casa Software Ltd., UK). The sp^3 peak of carbon was used for the calibration of all spectra and set to 285.00 eV.

2.4. Computational Details. For the prediction of the ground-state structure of small Hf_mO_n clusters (m and n corresponding to the number of Hf and O atoms, respectively), we utilized a global optimization method implemented as evolutionary algorithm in the USPEX code[27−30] combined with an all-electron-projector-augmented wave method as implemented in the Vienna ab initio simulation package (VASP).[31−33] In our calculations, clusters were separated by a 7 Å thick vacuum space. We used pseudopotentials with the following valence-electron configurations: $5s^25p^66s^05d^45f^0$ (with $4f^{14}$ electrons frozen in the core) for Hf, $2s^22p^4$ for O, and $2s^22p^2$ for C.[34] Exchange and correlation of electrons were taken into account using a generalized gradient approximation in the form of the Perdew−Burke−Ernzerhof (PBE) functional optimized for molecules.[35] The kinetic energy cutoff for the plane-wave basis set was limited to 600 eV. Structural optimization was performed until the Hellmann−Feynman force on each atom became less than 0.01 eV $Å^{-1}$. It is known that PBE is underestimating the highest occupied molecular orbital (HOMO)−lowest unoccupied molecular orbital (LUMO) gap. Therefore, to compare theoretical positions of the energy levels with available experimental spectroscopy data, the electronic structures for the selected clusters were calculated by the hybrid functional HSE06 with standard mixing and screening parameters.[36]

The structure prediction of nanoparticles started from randomly generated structures with various symmetries. All initial structures were relaxed. The next generations of structures were prepared using various mutation operators (heredity, random, periodic mutation, and soft mutation), applied to 60% of the lowest-energy structures taken from the previous step. The structure was considered as a ground state when it was not changed during a sufficiently large number of generations (typically 10 to 20 generations, depending on the cluster size).

In the calculations, we considered small clusters Hf_mO_n ($n = 2m \pm \delta$) and carbon-doped Hf_mO_n:C ($n = 2(m - 1) \pm \delta$) with m in the range of 3−10 and δ up to 7. The formation energy was evaluated as

$$\Delta G_f(T, p_{O_2}) = E(Hf_mO_n) - m\mu(Hf_{metal}) - n\mu_O(T, p_{O_2})$$

https://doi.org/10.1021/acsanm.2c04165
ACS Appl. Nano Mater. 2023, 6, 148−159

where $E(Hf_mO_n)$ is the ground-state total energy of the Hf_mO_n cluster, $\mu(Hf_{metal})$ is the chemical potential of Hf atoms in their metallic form, and $\mu_O(T,p_{O2})$ is the chemical potential of oxygen atoms. In equilibrium with molecular O_2 gas results: $\mu_O(T,p_{O2}) = 1/2\ [E(O_2) + \mu_{O2}(T,p^0) + k_BT\ \ln(p_{O2}/p^0)]$, where $E(O_2)$ is the calculated total energy of the O_2 molecule, k_B is the Boltzmann constant, p_{O2} is the oxygen partial pressure, p^0 is the atmospheric pressure, and T is the absolute temperature. The $\mu_{O2}(T,p^0)$ term includes the temperature dependence of vibrational and rotational degrees of freedom of the O_2 molecule, as well as contributions to the thermodynamic potential of spin degrees of freedom at atmospheric pressure. It is taken from NIST-JANAF thermochemical tables.[37] The $k_BT\ \ln(p_{O2}/p^0)$ term accounts for entropy contributions to the chemical potential of oxygen.

For clusters with a carbon atom, the formation energy was calculated as

$$\Delta G_f(T, p_{O2}) = E(Hf_mO_n{:}\ C) - m\mu(Hf_{metal}) - n\mu_O(T, p_{O2}) - \mu(C)$$

where $E(Hf_mO_n{:}C)$ is the total energy of Hf_mO_n clusters with one C atom, $\mu(C)$ is the chemical potential of C atoms, calculated near one carbon vacancy in the graphene layer. The remaining parameters are calculated as for pure clusters.

3. RESULTS AND DISCUSSION

3.1. HfO_2 Nanoislands Grown by van der Waals Epitaxy. HfO_2 nanoislands (sub-monolayer HfO_2 films) were deposited by PLD and quenched after deposition to freeze in non-equilibrium growth states or phases. The growth conditions, such as deposition rate and coverage, were adjusted, so that isolated nanoislands are formed. The growth was carried out in an argon atmosphere to prevent damage to the defect-free HOPG substrate by the otherwise highly energetic particles formed during the ablation process at low pressure (kinetic energy, E_k about 20 to 30 eV).[38] The employed conditions ensure a relatively low value of the kinetic energy of hafnium atoms (E_k(Hf) ~ 2 eV) estimated based on preceding evaluations of plume species,[38] and thus a low defect density of the HOPG substrate after HfO_2 deposition (see Figure S2). Figure 1a represents a schematic of the HfO_2 deposition and a typical sub-monolayer HfO_2 film on HOPG, investigated by STM. In the STM image (Figures 1b and S5), bright HfO_2 nanoislands with a diameter in the range of 2.1 nm up to 9.8 nm are observed on top of the dark appearing HOPG. The root mean square roughness, taken over a surface area of 200 nm × 200 nm without HOPG steps, is RMS ≈0.59 nm, which is comparable to sub-monolayer films of HfO_2 on HOPG or graphene deposited by ALD.[14]

The apparent height of the HfO_2 nanoislands with respect to the HOPG surface peaks at 0.57 ± 0.11 nm (Figure 1c,d) and only a few exceptions with island heights >0.85 nm are found. The nanoisland height is thus in agreement with the size of one HfO_2 unit cell, as defined by the lattice parameters (0.50−0.54 nm) of monoclinic and tetragonal HfO_2.[39,40] The distribution of the HfO_2 nanoisland areas (Figure 1e) emphasizes several particularly stable island sizes. Especially the areas of about 7.3 and 16.2 nm^2 are dominant for small islands, larger islands stabilize at about 27.3 and 37.3 nm^2. Assuming a height of one unit cell, these areas correspond to nanoislands of approximately 30, 65, 109, and 149 unit cells, pointing to stable subunits such as grains stabilizing at a size of about 30 unit cells. Larger islands are formed by agglomeration of multiple small islands at these deposition conditions only.

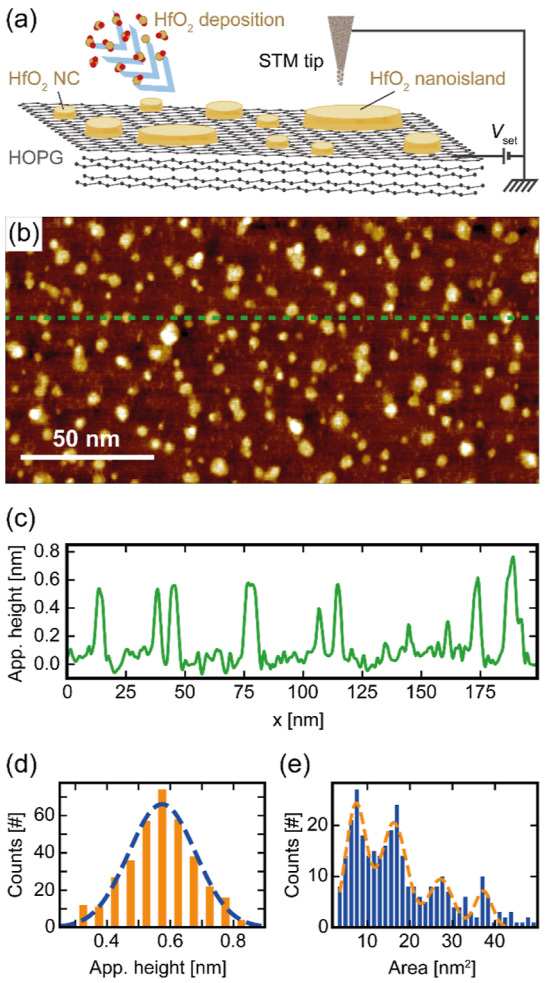

Figure 1. HfO_2 nanoislands on HOPG. (a) Schematic showing the principles of deposition and STM measurement of HfO_2 nanoislands on HOPG. (b) STM topography (size: 200 × 100 nm^2, V_{set} = 1.5 V, and I_{set} = 0.51 nA). (c) Apparent height along the dashed line in (b). (d) Apparent height distribution (based on 362 nanoislands). (e) Distribution of the surface areas for well-separated islands.

Using high-resolution LT-UHV-STM, in addition to the above-described HfO_2 nanoislands, the first nucleation states of HfO_2 are identified as NCs with distinct sizes (Figure 2,

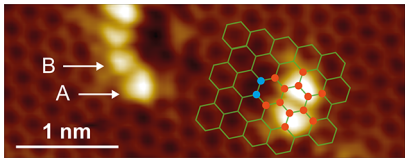

Figure 2. Representative LT-UHV-STM topography of HfO_2 NCs. The hexagonal lattice structure of HOPG is marked in green, carbon vacancies in the topmost layer in blue, and C atoms covered by the NCs in orange. NCs of two distinct sizes are marked by A and B. (V_{set} = −2.0 V; I_{set} = 88 pA).

more details in the Supporting Information, Figure S6). The areas of these NCs are well below 1 nm^2. NCs of type A have a triangular appearance from an aerial perspective and are slightly elongated in direction of a carbon vacancy. The length of the NC in this direction is l_A = (0.45 ± 0.02) nm, the width at the widest point is w_A = (0.33 ± 0.02) nm, and the apparent height is h_A = (0.092 ± 0.012) nm. The second identified type

https://doi.org/10.1021/acsanm.2c04165
ACS Appl. Nano Mater. 2023, 6, 148−159

of nuclei, type B, is always located next to a type A nucleus. With a length of l_B = (0.36 ± 0.01) nm, a width of w_B = (0.27 ± 0.01) nm, and an apparent height of h_B = (0.066 ± 0.010) nm, it is slightly smaller than type A. All dimensions of the NCs are obtained from STM topography images.

The HOPG background in Figure 2 displays its typical hexagonal lattice structure, and thus, individual missing C atoms can be identified. Usually, a small number of 2−4 HfO_2 nuclei are found to be located at the border of several combined carbon vacancies in the topmost layer of HOPG. Individual carbon vacancies can be created during the HfO_2 deposition process since the substrate was defect-free over wide ranges before, unlike observed here.

One possible source of vacancies in the topmost layer of HOPG is the ejection of C from the surface by incoming Hf atoms or HfO_x consisting of a few atoms. However, it should be noted that always conglomerates of several carbon vacancies are formed next to the grown NCs. This is a first hint toward an additional carbon consuming mechanism, which will be discussed below.

Since the growth of HfO_2 NCs, as indicated by STM images (Figure 2), is found to be accompanied by C vacancy formation in HOPG, XPS measurements were performed to check possible interactions between HfO_2 and carbon. The Hf 4f core level spectrum of HfO_2 nanoislands on HOPG (Figure 3) shows the characteristic splitting of 1.68 eV between the Hf

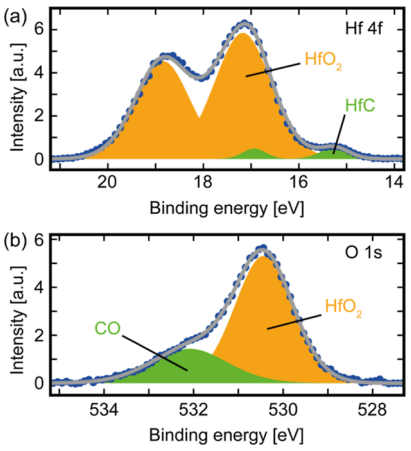

Figure 3. XPS core level spectra. (a) Hf 4f and (b) O 1s (blue dots correspond to the raw data and the gray line to the fit).

$4f_{7/2}$ peak and the Hf $4f_{5/2}$ peak. The main Hf $4f_{7/2}$ signal is found at a binding energy of 17.17 eV characteristic for bulk HfO_2. A small shoulder at 15.25 eV, visible in Figure 3a, is an indication for the formation of HfC.[41] Correspondingly, the O 1s spectrum exhibits a strong HfO_2 peak at 530.43 eV (Figure 3b) and a shoulder indicating the existence of CO at 532.10 eV. For comparison, HfO_2 nanoislands have been deposited on Au(111) using the same deposition parameters and inspected by XPS. In this case, no indication of HfC was determined (Supporting Information, Figure S7).

Based on these XPS results, the formation of HfC, which can be created during a carbothermic reduction: $HfO_2 + 3\ C \rightarrow HfC + 2\ CO$, should be taken into account. This reaction consumes three C atoms for the incorporation of one carbon into a mixed HfO_xC_y compound. Strictly speaking, the temperature of T = 650 °C in our PLD system should be too low for a completed chemical reaction.[21] On the other hand, additional energy is provided by the PLD process and a partial HfC formation is reported also for oxygen-deficient grown HfO_2 thin films during a vacuum annealing process at a temperature of T = 600 °C.[20] To further investigate the crystal nucleation and the interaction of HfO_2 with carbon from the topmost layer of HOPG, we employed an ab initio calculation to simulate the ground-state structures for a series of small HfO_2 clusters.

3.2. Nature of NCs. The structure of small Hf_mO_n nanoclusters and their formation energy was calculated up to a cluster size of m = 10 and n = 22 involving stoichiometric ($n = 2m$) and non-stoichiometric structures ($n = 2m \pm \delta$). In addition, doped Hf_mO_n:C, including one C atom, and $Hf_{10}O_n$:2C, containing two C atoms, were considered for comparison. The formation energy (scaled per atom) of pure (Hf_mO_n) and carbon-doped small hafnium oxide clusters (Hf_mO_n:C) is presented in Figure 4 as a function of their oxygen content, while the structures of selected clusters are given in Figure 5. All structures of the most stable pure Hf_mO_n clusters and clusters doped with one C atom, Hf_mO_n:C, can be found in Figure S8. The formation energy is decreasing with an increasing size of the clusters reflecting the smaller surface energy contribution for bigger clusters. The formation energy is expected to asymptotically approach the bulk value if m goes to infinity. Pure Hf_mO_n clusters show non-monotonic fluctuations in equilibrium stoichiometries: the most stable clusters with the number of Hf atoms m = 3, 6, 7, or 10, are stoichiometric, that is, Hf_3O_6, Hf_6O_{12}, Hf_7O_{14}, and $Hf_{10}O_{20}$, whereas the sub-stoichiometric clusters Hf_4O_7, Hf_5O_9, Hf_8O_{15}, and Hf_9O_{17} are found to be the most stable with m = 4, 5, 8, and 9. Especially in stoichiometric or oxygen-rich small clusters, apical oxygen atoms are found, namely, oxygen bound to one Hf atom only. In general, sub-stoichiometric clusters exhibit a more compact structure than the stoichiometric ones for small clusters (compare, for example, Hf_4O_6 and Hf_4O_8 in Figure 5). In addition, we find that larger clusters are often built from structural units of smaller ones, where the latter define the local order of atoms in the larger clusters (compare, for example, the structure of Hf_4O_6 and Hf_5O_9 in Figure 5).

The stability of clusters doped with carbon shows a crossover behavior in formation energy with respect to the pure clusters, where clusters Hf_5O_8:C, Hf_6O_{10}:C, Hf_7O_{12}:C, and Hf_9O_{16}:C are found to be more stable than the pure clusters with an equal amount of Hf atoms. Note that the energetically most favorable doped cluster with three and four Hf atoms, Hf_3O_8:C and Hf_4O_{10}:C, correspond to a Hf_3O_6 cluster and a Hf_4O_8 cluster, respectively, with a chemisorbed CO_2 molecule (Figures 5 and S8) and thus are not carbon doped. Notably, the structure of Hf_5O_8:C is considerably different from the most stable, pure Hf_5O_9 cluster, as a result of the incorporation of one C atom into the structural frame. Calculations of the charge density at the site of the incorporated C atom reveal a carbide-type character in agreement with the XPS results. Obviously, it is energetically more advantageous to incorporate a carbide-type C into a Hf5 cage or rather a Hf6 cage than to bridge the Hf atoms by two O atoms due to geometric restrictions. This view has been additionally verified by modeling the transition path for carbon migration from a graphene substrate with a pre-existing carbon vacancy to the Hf6 cage. (For details of the orientation of the Hf_6O_{10}:C cluster on the graphene surface, binding energy, or

https://doi.org/10.1021/acsanm.2c04165
ACS Appl. Nano Mater. 2023, 6, 148−159

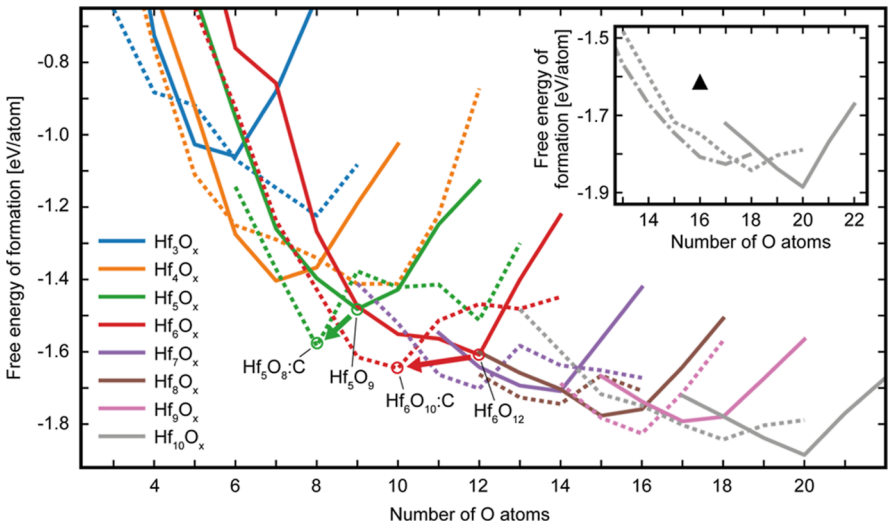

Figure 4. Formation energy (scaled per atom) as a function of oxygen content for clusters with different amounts of Hf atoms, calculated under experimental conditions (T = 650 °C; $p_{O2} = 10^{-8}$ mbar). Solid, dashed, and dot-dashed lines correspond to pure, carbon-doped, and twice carbon-doped clusters, respectively. Inset: Formation energy of pure and carbon-doped clusters with 10 Hf atoms. The black triangle marks the energetic position of the weakly bonded Hf_6O_{10}:C + Hf_4O_6 cluster (Figure S8).

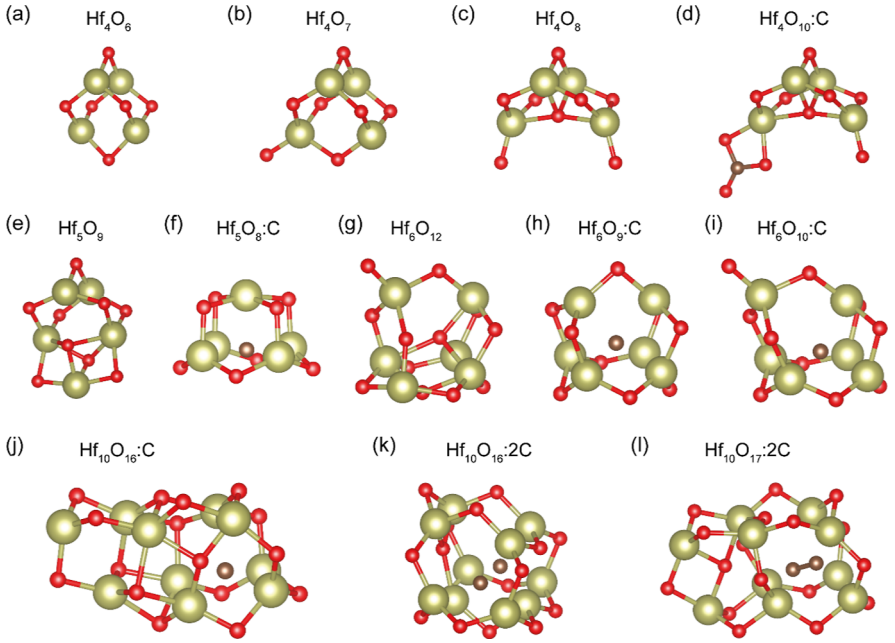

Figure 5. (a–l) Calculated stable structures of small hafnia clusters as indicated above the clusters (see also Figure S8 for additional cluster structures).

carbon incorporation, see Supporting Information, Chapter (V), Figures S9–S11.)

The carbon-doped clusters with more than six Hf atoms reveal often basic structural units of either Hf_6O_{10}:C or Hf_6O_9:C, containing one C atom and additional Hf_mO_n, attached to the basic unit frame. The structure of Hf_6O_9:C is very similar to the ground-state structure Hf_6O_{10}:C but without polar distortion, which is induced by the apical O atom (Figure 5). The formation energy of Hf_7O_{12}:C is only marginally smaller than the one of pure Hf_7O_{14}. Regarding the stability of larger clusters, doping with carbon is not necessarily energetically favorable with respect to the undoped case. Thus, our calculations reveal that the incorporation of carbide-type carbon is especially advantageous for Hf_mO_n clusters with five or six Hf atoms, while it is insignificant for the other nanoclusters under investigation. For comparison, we also calculated the ability of $Hf_{10}O_x$ clusters to incorporate two C atoms and found that the most stable $Hf_{10}O_{17}$:2C cluster incorporates a C–C pair into a Hf8 frame (Figures 4 and 5). On the other side, the $Hf_{10}O_{16}$:2C cluster incorporates two single C atoms in two Hf6-like frames and thus resembles two merged Hf_6O_{10}:C units which are sharing two Hf atoms. In both cases, the formation energy is higher than for the pure $Hf_{10}O_{20}$ or the singly doped $Hf_{10}O_{18}$:C case, making the realization of the twice carbon-doped Hf10 cluster unfavorable.

Comparing the experimentally determined HfO_2 nuclei from STM measurements with the modeled Hf_mO_n clusters, we find that the smaller nuclei B correspond in size and shape to

https://doi.org/10.1021/acsanm.2c04165
ACS Appl. Nano Mater. 2023, 6, 148–159

clusters with four Hf atoms, while the somewhat larger nuclei A fit to the clusters with six Hf atoms. The absence of smaller clusters in experimental STM images and the considerably higher formation energy of clusters with three Hf atoms let us assume that these clusters are not stable under our growth conditions with respect to Hf_4O_x clusters. The most stable cluster containing four Hf atoms is Hf_4O_7, as discussed above, while Hf_6O_{10}:C is the composition of the cluster corresponding to nucleus A. We assume that the reaction leading to the latter carbon-containing cluster is carbothermic reduction. In order to check this possibility, we also calculated the reaction enthalpy for the reaction: $Hf_mO_n + 3\ C \rightarrow Hf_mO_{n-2}{:}C + 2\ CO$. The reduction is spontaneous, that is, the reaction is exothermic, for stoichiometric or oxygen-rich Hf_mO_n clusters [see Supporting Information, Chapter (VI)]. Taking Hf_5O_x as an example, the carbothermic reduction is exothermic for clusters with at least 10 O atoms. Comparing Hf_5O_{10} with the reaction product Hf_5O_8:C, as well as Hf_6O_{12} with Hf_6O_{10}:C, the incorporation of carbon is beneficial. Toward larger cluster sizes, the release of reaction enthalpy decreases considerably, and approaching bulk HfO_2, the reduction will not be more favorable. Consequently, the incorporation of carbide-type carbon is most favorable during crystal nucleation in order to grow HfO_2 nanoislands or thin films, while it becomes less important for the further growth of bulk structure. The herein-described carbon incorporation into small hafnia-based structures is an important issue for growth processes that provide a carbon source at the early growth states (e.g., graphene as substrate for special applications) or during the deposition of an amorphous HfO_2 layer, like the ALD process which is based on organic compounds.

Inspired by the chains of NCs in Figure 2, we also started to model the formation energy and the electronic structure of combinations of clusters, that is, combinations of the Hf_6O_{10}:C cluster (considered as the basic unit frame) linked together with pure small ones. We found that the best match with experimental data is obtained when we assume the Hf_6O_{10}:C cluster is weakly bonded to a pure Hf_4O_6 cluster. The term weakly bonded describes here the interaction between both clusters. They share three O atoms, but they still exhibit their original cluster cages in contrary to the $Hf_{10}O_{16}$:C cluster in the ground state with a full rearrangement of atoms (Figures 5 and S8). The formation energy of this weakly bonded configuration is depicted by a black triangle in the inset of Figure 4. It is somewhat higher than the formation energy of the corresponding $Hf_{10}O_{16}$:C ground state cluster, which has the same stoichiometry. However, a substantial gain of energy compared to the isolated Hf_6O_{10}:C and Hf_4O_6 cluster is obtained. Thus, we suggest that the observed weakly bonded chains of NCs are intermediate growth states detectable due to the quenching of the samples immediately after deposition.

Beside the chains composed of type A and type B NCs, a motive of two neighboring type A NCs is observed in Figure 2. This motive is recurring with the same orientation relative to the substrate and is located next to the same carbon vacancy assembly. To simulate the experimental constant current STM image, we calculated the partial electronic charge density distribution for the states below the Fermi level in an energy window matching experimental bias. In order to unambiguously identify the structure of these type A NCs, STM image simulations were performed considering two neighboring Hf_6O_{10}:C clusters which were oriented relative to the substrate, as shown in Figure S9, right side. As substrate graphene with a double carbon vacancy next to the clusters was used. Interestingly, Hf and O atoms belonging to the neighboring Hf_6O_{10}:C clusters formed four extra bonds during relaxation connecting the two clusters together. This resulting new configuration fits the STM image quite reasonably (see Figure S12). However, relevant electronic states, suitable to represent the experimental STM images, could be highlighted only in an enlarged energy interval [for details, see Supporting Information, Chapter (VII)].

In another approach of modeling two neighboring type A NCs, as identified in the STM image, the $Hf_{10}O_{16}$:2C cluster (Figure 5k) was employed, which corresponds to the two merged Hf_6O_{10}:C clusters that are sharing one face. Here, the resulting calculated partial charge density distribution ideally meets the brightest lobes in the STM image considering the energy range from E_F to −2.3 eV (Figures 6 and S13).

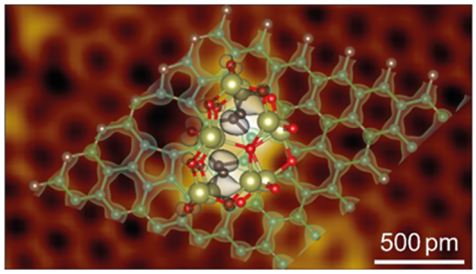

Figure 6. Overlay of the experimental STM image of two type A NCs located next to each other and the theoretical structure of the $Hf_{10}O_{16}$:2C cluster near a double carbon vacancy in the graphene substrate, together with the partial charge density isosurface for the electronic states of the cluster and the graphene surface in the range from the Fermi level to −2.3 eV (see also Supporting Information, Figure S13).

Moreover, states located on the peripheral O atoms perfectly match all small features of the contour of the experimental STM data pointing to an excellent agreement with the predicted structure of the $Hf_{10}O_{16}$:2C nanocluster. The fact that the structure of the metastable $Hf_{10}O_{16}$:2C cluster fits experimental STM images best points to the importance of kinetic processes during the growth of clusters which are probably, starting with the nucleation of the Hf_6O_{10}:C clusters. The driving force for further crystal growth or the merging of neighboring clusters is the enlarged stabilization energy of bigger Hf_mO_n:C clusters.

3.3. Electronic Properties of HfO_2 Nanoislands. The semiconductor properties of the HfO_2 nanoislands were investigated by STS. In total, 152 $I-V$-curves and the related dI/dV-signals were taken for various TSS defined by the respective set voltage at a constant set current (I_{set} = 0.51 nA). The dI/dV spectra for V_{set} from −2.50 to −5.00 V are shown in Figure 7. The onset of the differential conductance at negative biases marks the valence band maximum (VBM), and that at positive biases marks the conduction band minimum (CBM). Here, we determine the energies of the band edges (E_{VBM} and E_{CBM}) and the apparent band gap (E_G) for large TSS (V_{set} = −4.00 to −5.00 V) from the logarithmic dI/dV-signal according to the method given in M. Ugeda et al.[25] Exemplarily, the mean of five current−voltage ($I-V$) curves and the logarithmic differential conductance [$\log(dI/dV)$] signal are graphed in Figure 7b (see Figure S14 for details). By evaluating 31 spectra, we obtained the mean values E_{VBM} =

https://doi.org/10.1021/acsanm.2c04165
ACS Appl. Nano Mater. 2023, 6, 148−159

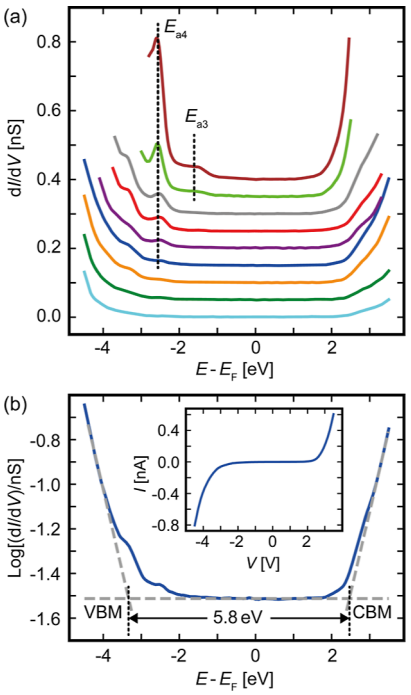

Figure 7. STS on HfO_2 nanoislands on HOPG. (a) dI/dV-signal for varying TSS (E_F is the Fermi level defined by HOPG; I_{set} = 0.51 nA). V_{set}, from top to bottom: −2.50 V (brown), −3.00 V (lime), −3.50 V (gray), −3.75 V (red), −4.00 V (purple), −4.25 V (blue), −4.50 V (orange), −4.75 V (green), and −5.00 V (cyan). For clarity, the curves are shifted in the y-direction by 0.05 nS. In-gap acceptor states (E_{ax}) are marked with vertical dashed lines. (b) Logarithmic differential conductance spectrum [log(dI/dV)] corresponding to the blue curve in (a). Inset: corresponding I−V curve.

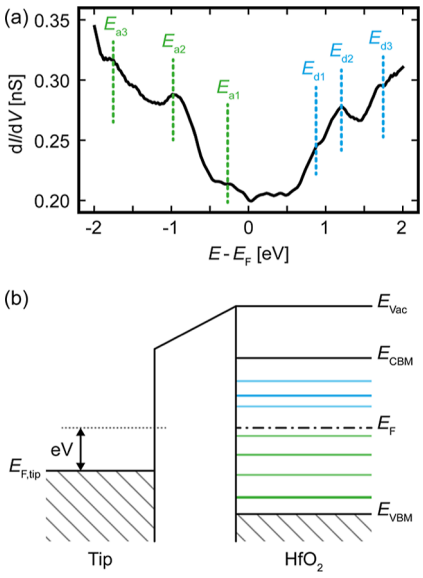

Figure 8. In-gap states obtained from HfO_2 nanoislands. (a) Representative dI/dV curve showing acceptor-type (E_a, green) and donor-type (E_d, blue) states (V_{set} = −1.5 V and I_{set} = 0.51 nA). (b) Schematic band diagram deduced from STS data.

(−3.23 ± 0.08) eV, E_{CBM} = (2.56 ± 0.11) eV and the size of the apparent band gap E_G = (5.78 ± 0.13) eV. The latter is in great agreement with other crystalline thin films and bulk monoclinic HfO_2,[8,42,43] that is, one unit cell high HfO_2 nanoislands with an area down to about 30 unit cells, or with a diameter of roughly 3 nm, already exhibit a bulk-like band gap.

For decreasing TSS, the above-described band onsets contribute strongly to the differential conductance signal, and a shoulder-like peak, appearing at the valence band edge, is attributed to the oxygen band of bulk HfO_2. Similarly, a shoulder in the differential conductance corresponding to the conduction band edge is allocated to the hafnia band of bulk HfO_2. Further approaching the tip toward the HfO_2 nanoislands, a very pronounced acceptor state at E_{a4} = (−2.58 ± 0.05) eV and a state at E_{a3} = (−1.75 ± 0.04) eV are measured in the band gap. These states clearly gain intensity with decreasing TSS, dominate the dI/dV signal in Figure 7a, and inhibit the measurement of spectra over wide voltage ranges for small TSS since their current contribution exceeds the current limitation of the STM/STS system under these conditions.

For the smallest TSS, corresponding to set voltages from −1.0 to −2.0 V, additional electronic states are recorded within the band gap of HfO_2 nanoislands (Figure 8). While E_{a3} was already observed in Figure 7a, two additional states are identified under these conditions, an acceptor state at E_{a2} = (−1.03 ± 0.05) eV and a donor state at E_{d2} = (1.19 ± 0.05) eV, while a minor intense but recurring electronic state is located at E_{a1} = (−0.30 ± 0.08) eV. In addition, two shoulders appear at E_{d1} = (0.84 ± 0.05) eV and E_{d3} = (1.74 ± 0.03) eV. It should be noted that for bulk HfO_2, two defect bands are known,[43] which are located 1.44 and 2.81 eV below the conduction band edge and perfectly correspond to the peaks in the differential conductance curves labeled with E_{d2} and E_{a1}, respectively, pointing again to the bulk-like properties of the nanoislands.

The origin of additional states appearing within the band gap of semiconductors may be intrinsic surface states, defect states, or tip-induced band bending (TIBB). TIBB is a common source of errors when determining the position of the band edges. A metallic tip in proximity to a semiconducting surface can cause a change in the electrostatic potential.[44] Thus, a charge carrier accumulation or depletion zone can be induced, which subsequently leads to additional current contributions within the band gap, especially if E_F is close to a band edge. In consequence, the size of the band gap is reduced with decreasing TSS.[22] However, this is not the case for our measurements. Here, the states in the spectra of Figure 7 are fixed and the Fermi level is far (>2.5 eV) from the band edges. Since the size of the band gap is almost constant for large TSS, we can surely rule out TIBB and assume a flat band condition.

Thus, the additional in-gap current contributions can be caused by intrinsic surface states or defect states. Both are characterized by peaks in the differential conductance spectra. As shown in previous investigations, surface states or defect-related currents are sensitive to the TSS[22,23] and usually increase with decreasing TSS, as observed here. In the case of the HfO_2 nanoislands, which offer a high step-edge density, intrinsic oxygen vacancies, and interstitials, the assignment of the in-gap states is non-trivial. In addition, the observed carbon incorporation, as discussed above, may lead to in-gap states. Therefore, we will discuss the experimentally obtained in-gap states in comparison with the theoretical investigations of model clusters.

3.4. Assignment of Electronic In-Gap States. We have calculated the electronic structure for all stable Hf_mO_n and

https://doi.org/10.1021/acsanm.2c04165
ACS Appl. Nano Mater. 2023, 6, 148−159

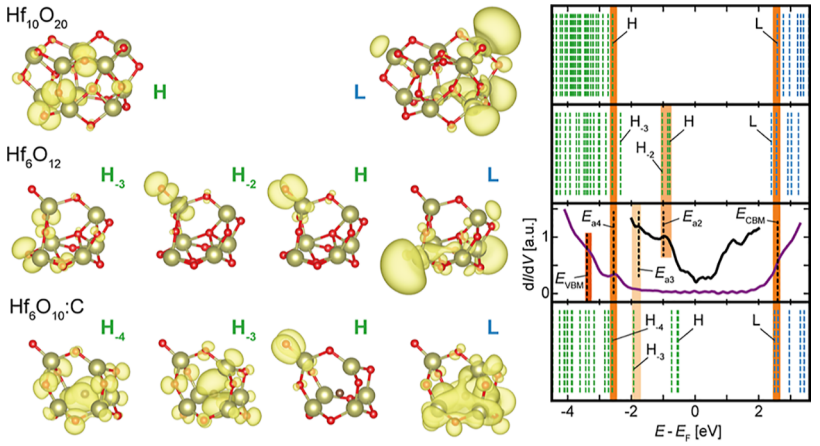

Figure 9. Right side: energy positions and partial electron densities of calculated electronic states for the clusters: $Hf_{10}O_{20}$, Hf_6O_{12}, and Hf_6O_{10}:C, indicated by vertical dashed green and blue lines, in comparison to experimental differential conductance curves on HfO_2 islands (H is the short form for HOMO, H_{-x} stands for HOMO-X, and L is the short form for LUMO). Experimentally observed in-gap states as well as the band onsets (abbreviations are same as in Figures 7 and 8) are marked with black vertical dashed lines in the dI/dV curves. Orange vertical stripes mark the corresponding experimental and calculated states. To compare the calculated electronic structure of the clusters with the STS data, the bulk-like unoccupied Hf-states were aligned with E_{CBM}, with exceptions for small clusters with bulk-like oxygen and hafnium-related states, both in the range of E_{a4} to E_{CBM}. Left side: isosurface plots (charge density) corresponding to the marked electronic states.

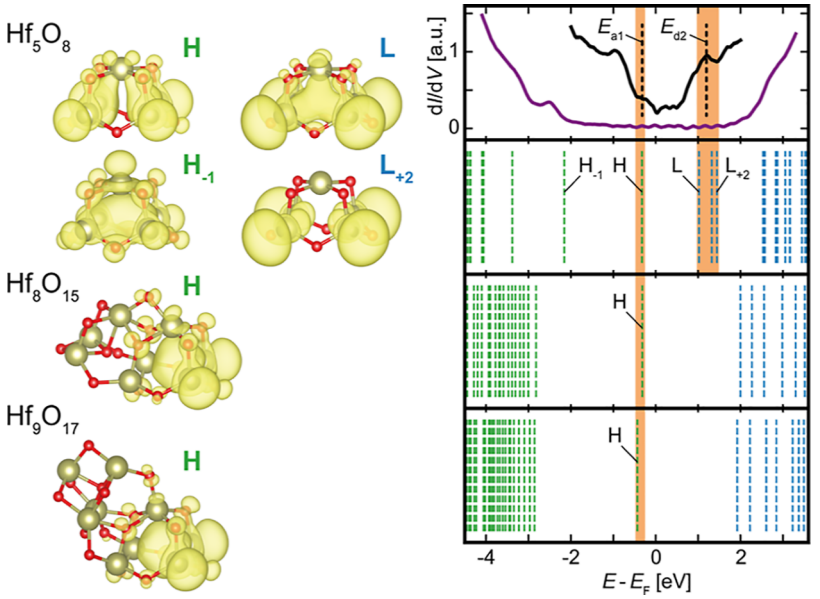

Figure 10. Characteristic electronic states of representative sub-stoichiometric hafnia clusters. Left side: isosurface plots (charge density) of selected states. Right side: energy positions in comparison with experimentally deduced in-gap states from dI/dV curves. Color code and abbreviations used are similar to that in Figure 9. For the Hf_mO_{n-x} clusters given here, the theoretically derived energy positions are given as calculated without any shift.

Hf_mO_n:C nanoclusters as well as for all clusters, which might correspond to the depicted NCs in Figure 2 from a topological point of view. In Figure 9, the partial charge density of the states around the Fermi level of selected stoichiometric nanoclusters, which all exhibit a diameter well below 1 nm, is given in comparison to the experimental differential conductance curve obtained from nanoislands. It should be mentioned that each pronounced correlation between the energetic state and the cluster structure element, which will be discussed in the following, has been observed on several nanoclusters. Here, we intentionally refrain from the discussion of interacting effects and present the most distinct examples in Figures 9 and 10 (see the Supporting Information for more complex examples: Figures S15 for Hf_4O_7 and weakly bonded Hf_6O_{10}:C + Hf_4O_6).

For the largest stoichiometric cluster under consideration, $Hf_{10}O_{20}$, the HOMO is delocalized over 14 O atoms, while the LUMO is delocalized over hafnium atoms, resulting in a calculated HOMO−LUMO gap of 5.17 eV. Already for this cluster size, a wide electronic gap is obtained and the frontier orbitals are built, like in bulk HfO_2, by delocalized orbitals over oxygen or hafnium atoms. A comparison of the calculated HOMO($Hf_{10}O_{20}$) and LUMO($Hf_{10}O_{20}$) with the STS data reveals that these frontier orbitals correspond to prominent states identified in the dI/dV curves, which were denoted as E_{a4} = −2.58 eV and E_{CBM} = 2.56 eV, respectively (Figure 9). This leads to the finding that the energy of the CBM is already

https://doi.org/10.1021/acsanm.2c04165
ACS Appl. Nano Mater. 2023, 6, 148−159

approached by delocalized orbitals over hafnium atoms in a $Hf_{10}O_{20}$ cluster, with Hf atoms coordinated by four O atoms each. On the other hand, since small $Hf_{10}O_{20}$ clusters are exclusively composed of surface oxygens, E_{a4}, measured as an in-gap state on HfO_2 nanoislands, can be identified as surface state resulting from O atoms bridging two hafnium atoms.

Looking at the smaller Hf_6O_{12} cluster, we find a diminished delocalization of the oxygen and hafnium states, respectively. In addition, this cluster exhibits another specialty. Here, electron densities mainly located at an apical oxygen show up that give rise to states around −1.0 eV corresponding to a peak in the STS curve labeled E_{a2}. These states are attributed to surface oxygens with a high electron density which are only bound to one hafnium atom. It can be assumed that these singly bound O atoms can be found on grain boundaries or nanoisland surfaces after growing under stoichiometric conditions as well as after forming oxygen vacancies and oxygen movement to the surface. The carbon-doped Hf_6O_{10}:C cluster exhibits these apical oxygen states as well, but here they are shifted toward E_F due to an additional state around −1.93 eV. This additional state, denoted as H_{-3} in the partial charge density plot for Hf_6O_{10}:C in Figure 9, arises from a delocalized state over the carbide-type carbon as well as oxygen and hafnium atoms. It corresponds roughly to E_{a3} found in STS curves and is attributed to a carbon-related defect state. It should be noted that even though the H and L states are very localized in these clusters, in principle, no charging can be observed during STM/STS measurements, since for clusters in direct contact with a conducting substrate, the lifetime of the charged state is too short to be observed within the possible time resolution of a STM system. So far, the distinct in-gap states E_{a4} to E_{a2} determined from STS investigations could be assigned to oxygen surface states or a carbon-related defect state as demonstrated here for different stoichiometric Hf_mO_n or Hf_mO_n:C clusters. However, the two remaining distinct states E_{a1} and E_{d2}, which correspond to defect states as determined in bulk HfO_2, can only be found in sub-stoichiometric clusters, as shown in Figure 10. For clarity, only sub-stoichiometric Hf_mO_n clusters without carbon will be discussed.

For the sub-stoichiometric Hf_5O_8 cluster, we find a distinct state −0.32 eV below E_F (H). This orbital is largely delocalized over the highly symmetrical frame of the Hf_5O_8 cluster, consisting of one fourfold coordinated Hf and four threefold coordinated Hf. The corresponding unoccupied orbital (L) is located together with orbitals related to the four threefold coordinated Hf at energies around 1.2 eV. Thus, the states E_{a1} and E_{d2} determined from differential conductance measurements and previously described as defect bands[43] can be attributed to the presence of threefold coordinated hafnium atoms. This is very obvious, especially for the HOMO just below E_F (E_{a1}), which is also observed in an analogous kind in larger sub-stoichiometric Hf_mO_n clusters based on the Hf_5O_8 structural unit, as shown in Figure 10. In Hf_8O_{15} as well as in Hf_9O_{17}, the HOMO is largely delocalized mainly over the threefold coordinated Hf atoms. The corresponding LUMOs are anti-bonding counterparts of the HOMO states and are localized on atoms of the Hf_5O_8 structural unit. The gap is increased due to the stronger localization of the LUMO states in the presence of additional atoms.

Again, regarding the stability variations of doped/undoped clusters with the same number of Hf atoms, these results provide additional insights. The basic structure Hf_5O_8 can be stabilized by incorporation of one carbon into the cage, resulting in Hf_5O_8:C. The energy gain of 0.18 eV/atom is based on the ability of carbon to coordinate to four Hf atoms at the same time, which are only threefold coordinated by oxygen. The carbon-doped Hf_5O_8:C cluster exhibits even an enlarged stability compared to the most stable undoped cluster with five Hf atoms, Hf_5O_9, since in the latter threefold coordinated Hf remain due to structural limitations (see the green arrow $Hf_5O_9 \rightarrow Hf_5O_8$:C in Figure 4).

What does this discussion mean for nanocrystalline HfO_2, where grain boundaries play a major role as sinks for defects which are promoting electrical conductance or atomic diffusion? In crystalline HfO_2, each Hf atom is coordinated with seven oxygen, and each oxygen is coordinated with three or four Hf atoms. These are clearly higher coordination numbers than possible in small Hf_mO_n clusters. However, if a neutral oxygen vacancy is generated in crystalline HfO_2, an energy level occupied by two electrons is introduced into the band gap, which is mainly localized on adjacent Hf atoms.[45,46] In case that these oxygen vacancies and/or the O atoms segregate toward the grain surfaces in nanocrystalline HfO_2, as observed at an elevated temperature, the resulting grain boundary structure will exhibit structural elements that can be compared to our small Hf_mO_n clusters. In this work, identified, oxygen-deficient or oxygen-surplus structural units may also be formed at grain surfaces of nanocrystalline HfO_2 (or, possibly, in the amorphous state) and contribute to an increased electrical conduction and atomic diffusion. The here-characterized structural units give rise to the following in-gap states: (i) the defect state attributed to threefold coordinated Hf atoms (E_{d2}), (ii) the delocalized state just below E_F (E_{a1}), (iii) the defect state induced by the incorporation of carbide-type carbon (E_{a3}), as well as (iv) the surface states attributed to apical oxygens (E_{a2}) or (v) Hf-bridging oxygens (E_{a4}). The two oxygen-related defect states, E_{a1} and E_{d2}, here identified by (i) the partial charge density of sub-stoichiometric Hf_mO_n clusters (clusters based on the Hf_5O_8 structural unit and Hf_4O_7) and (ii) the differential conductivity measurements on nanocrystalline HfO_2 nanoislands correspond well to defect bands referred in the literature as deep (2.81 eV below E_{CBM}) and shallow defects (1.44 eV below E_{CBM}) in oxygen-deficient HfO_2, as discussed above.[43] They have been calculated theoretically for crystalline HfO_2 as well as identified experimentally in nanocrystalline HfO_2.[43] Moreover, the H-state of Hf_4O_7 clusters (Supporting Information, Figure S15), which originates from the uncompensated charge of Hf cations, shows the same topology as recently reported in-gap states of tetragonal sub-stoichiometric Hf_4O_7 in the energy range from −2 eV to E_F (Supporting Information, Figure S16).[47] The latter are also represented by uncompensated charge from neighboring Hf atoms, localized on bonding-like orbitals at the places of oxygen vacancies. In addition, the anti-bonding counterparts, that is, unoccupied in-gap states in crystalline tetragonal Hf_4O_7 in the energy range from the Fermi level up to 1.9 eV are similar by topology to the L-state of the Hf_4O_7 nanocluster. This similarity, both structural and electronic, indicates that the Hf_4O_7 cluster is the smallest representative of sub-stoichiometric tetragonal Hf_4O_7 hafnia. The crystalline structures of all discussed clusters are collected in Supporting Information, Chapter (X).

The switching performance in ReRAM devices can be settled experimentally by the variation of the non-stoichiometry of HfO_x thin films by modulating the oxygen flow during

https://doi.org/10.1021/acsanm.2c04165
ACS Appl. Nano Mater. 2023, 6, 148−159

deposition, by the selection of the electrode material, or the application of doping.[5,8,12,16] However, following the idea of ultimate scaling to its end, it is necessary to control these desired deviations from the ideal HfO_2 crystal structure at the atomic level. The here-presented results indicate a way for the fine-tuning of in-gap states based on oxygen defects or carbon doping in smallest nanoislands or NCs. Since the presence of deep or shallow in-gap defect states plays a significant role with respect to electron conduction in memristive devices as well as for the electroforming step,[48] they will directly affect the device resistance. The here-applied growth conditions for HfO_2 nanoislands on HOPG, resulting in carbide-type carbon (E_{a3}) incorporation, can be transferred likewise to HfO_2 NCs on graphene, a substrate which is discussed for ReRAM devices.[17] On the other hand, oxidizable substrates used in ReRAM like, for example, Hf or Ti,[5] are expected to promote the creation of oxygen-deficient HfO_2 nanoclusters exhibiting E_{a1} and E_{d2} in-gap states. The here-presented methodology might be advantageously employed to identify which stoichiometric, oxygen-deficient, or oxygen-surplus HfO_2 nanoclusters will be the most stable under the respective growth conditions.

4. CONCLUSIONS

In conclusion, the topographic and electronic properties of HfO_2 nanoislands, grown by PLD via van der Waals epitaxy, are investigated by LT-UHV-STM and STS taking advantage of real-space imaging and access to atomic-scale electronic properties. Thus, stable nanoislands with a height of one unit cell and an area of 7 nm^2 were identified to show an apparent band gap of 5.8 eV, comparable to the value of bulk material and indicating an ultimate scaling potential for ReRAM. Furthermore, HfO_2 NCs with dimensions below 0.5 nm were determined by atomically resolved STM. Combining theoretically predicted crystalline structures of lowest-energy clusters with the experimental STM images, these tiny NCs were identified as Hf_6O_{10}:C (as well as $Hf_{10}O_{16}$:2C corresponding to two merged Hf6-like frames) and Hf_4O_7 clusters. They preferentially nucleate under the experimental conditions used in this work. Together with Hf_5O_8 and Hf_5O_8:C, these clusters build concurrently basic structural frames that recur in larger clusters. Under the applied growth conditions, the incorporation of carbide-type C atoms during crystal nucleation is energetically favorable over the formation of pure Hf_mO_n clusters for selected cluster sizes with m = 5, 6. In addition, this carbon incorporation is a source for an in-gap state observed for small Hf_mO_n clusters. Combining differential conductance spectroscopy with ab initio hybrid-functional calculations of the electronic states, the origin of further surface and defect-related in-gap states was determined. Thus, two surface states were attributed to (i) a delocalized state over O atoms bridging two hafnium atoms and (ii) apical oxygen singly bound to a Hf atom, respectively. On the other hand, two defect states, represented by (i) a largely delocalized orbital with an energy somewhat below E_F(HOPG) and (ii) an unoccupied orbital delocalized over threefold coordinated hafnium atoms in sub-stoichiometric Hf_mO_n clusters, were related to defect states resulting from the formation of oxygen vacancies in HfO_2 nanoislands. These latter defect states correspond well to defect bands referred as deep and shallow defects in oxygen-deficient HfO_2 thin films typically used in ReRAM devices. Thus, our model system formed by basic structural Hf_mO_n(:C) frames will provide meaningful contributions to the discussion of the impact of oxygen vacancies or doping with carbon on the performance of memory devices based on (poly)crystalline or amorphous hafnia in the vicinity of the ultimate scaling limit.

■ ASSOCIATED CONTENT

Supporting Information

The Supporting Information is available free of charge at https://pubs.acs.org/doi/10.1021/acsanm.2c04165.

PLD growth; STM/STS analysis; XPS of HfO_2 nanoislands; structures of stable small HfO_2 clusters; simulations of Hf_6O_{10}:C on graphene; in-gap state calculations; and STM image simulation (PDF)

■ AUTHOR INFORMATION

Corresponding Authors

Konstantin Z. Rushchanskii − *Peter Grünberg Institute (PGI-1) and Institute for Advanced Simulation (IAS-1), Forschungszentrum Jülich GmbH and JARA, 52425 Jülich, Germany;* orcid.org/0000-0003-3070-5725; Email: k.rushchanskii@fz-juelich.de

Silvia Karthäuser − *Peter Grünberg Institute (PGI-7) and JARA-FIT, Forschungszentrum Jülich GmbH, 52425 Jülich, Germany;* orcid.org/0000-0003-3953-6980; Email: s.karthaeuser@fz-juelich.de

Authors

Niclas Schmidt − *Peter Grünberg Institute (PGI-7) and JARA-FIT, Forschungszentrum Jülich GmbH, 52425 Jülich, Germany; Faculty 1−Mathematics, Computer Science and Natural Science, RWTH Aachen University, 52062 Aachen, Germany;* orcid.org/0000-0002-8439-8495

Urška Trstenjak − *Peter Grünberg Institute (PGI-7) and JARA-FIT, Forschungszentrum Jülich GmbH, 52425 Jülich, Germany;* orcid.org/0000-0002-9447-1502

Regina Dittmann − *Peter Grünberg Institute (PGI-7) and JARA-FIT, Forschungszentrum Jülich GmbH, 52425 Jülich, Germany*

Complete contact information is available at: https://pubs.acs.org/10.1021/acsanm.2c04165

Author Contributions

S.K. planned the experiments. U.T. and N.S. performed PLD experiments. N.S. conducted the STM/STS and XPS experiments and all analyses. K.Z.R. planned and executed the DFT calculations. N.S., K.Z.R., and S.K. wrote the manuscript with contributions of all authors. All authors have given approval to the final version of the manuscript.

Notes

The authors declare no competing financial interest.

■ ACKNOWLEDGMENTS

The authors gratefully acknowledge the assistance of Stephan Aussen in XPS and the technical help of Jochen Friedrich and Stephan Masberg. K.Z.R. acknowledges fruitful discussions with Nicolae Atodiresei. This work was funded by Deutsche Forschungsgemeinschaft (DFG) through SFB 917 "Nanoswitches". K.Z.R. gratefully acknowledges the computing time granted by the Jülich-Aachen Research Alliance (JARA) Vergabegremium and provided on the JARA Partition part of the supercomputer JURECA[49] at Forschungszentrum Jülich and JARA-HPC Partition (Project no. jara0126) as well as the

support by Joint Lab Virtual Materials Design (JLVMD). Visualization was made with the help of the VESTA code.[50]

REFERENCES

(1) Waser, R.; Dittmann, R.; Staikov, G.; Szot, K. Redox-based resistive switching memories - Nanoionic mechanisms, prospects, and challenges. *Adv. Mater.* **2009**, *21*, 2632−2663.
(2) Cueppers, F.; Menzel, S.; Bengel, C.; Hardtdegen, A.; von Witzleben, M.; Boettger, U.; Waser, R.; Hoffmann-Eifert, S. Exploiting the switching dynamics of HfO_2-based ReRAM devices for reliable analog memristive behavior. *APL Mater.* **2019**, *7*, 91105/1−9.
(3) Cheema, S. S.; Kwon, D.; Shanker, N.; Dos Reis, R.; Hsu, S. L.; Xiao, J.; Zhang, H.; Wagner, R.; Datar, A.; McCarter, M. R.; Serrao, C. R.; Yadav, A. K.; Karbasian, G.; Hsu, C. H.; Tan, A. J.; Wang, L. C.; Thakare, V.; Zhang, X.; Mehta, A.; Karapetrova, E.; Chopdekar, R.; Shafer, P.; Arenholz, E.; Hu, C.; Proksch, R.; Ramesh, R.; Ciston, J.; Salahuddin, S. Enhanced ferroelectricity in ultrathin films grown directly on silicon. *Nature* **2020**, *580*, 478.
(4) Lee, H. J.; Lee, M.; Lee, K.; Jo, J.; Yang, H.; Kim, Y.; Chae, S. C.; Waghmare, U.; Lee, J. H. Scale-free ferroelectricity induced by flat phonon bands in HfO_2. *Science* **2020**, *369*, 1343.
(5) Banerjee, W.; Kashir, A.; Kamba, S. Hafnium oxide (HfO_2) - A multifunctional oxide: A review on the prospect and challenges of hafnium oxide in resistive switching and ferroelectric memories. *Small* **2022**, *18*, 2107575.
(6) Materlik, R.; Künneth, C.; Kersch, A. The origin of ferroelectricity in $Hf_{1-x}Zr_xO_2$: A computational investigation and a surface energy model. *J. Appl. Phys.* **2015**, *117*, 134109.
(7) Cavalieri, M.; O'Connor, E.; Gastaldi, C.; Stolichnov, I.; Ionescu, A. M. Experimental investigation of pulsed laser deposition of ferroelectric Gd:HfO_2 in a CMOS BEOL compatible process. *ACS Appl. Electron. Mater.* **2020**, *2*, 1752−1758.
(8) Sharath, S. U.; Vogel, S.; Molina-Luna, L.; Hildebrandt, E.; Wenger, C.; Kurian, J.; Duerrschnabel, M.; Niermann, T.; Niu, G.; Calka, P.; Lehmann, M.; Kleebe, H. J.; Schroeder, T.; Alff, L. Control of switching modes and conductance quantization in oxygen engineered HfOx based memristive devices. *Adv. Funct. Mater.* **2017**, *27*, 1700432/1−13.
(9) Dittmann, R.; Strachan, J. P. Redox-based memristive devices for new computing paradigm. *APL Mater.* **2019**, *7*, 110903/1−10.
(10) Wang, Y.; Niu, G.; Wang, Q.; Roy, S.; Dai, L.; Wu, H.; Sun, Y.; Song, S.; Song, Z.; Xie, Y. H.; Ye, Z. G.; Meng, X.; Ren, W. Reliable resistive switching of epitaxial single crystalline cubic Y-HfO_2 RRAMs with Si as bottom electrodes. *Nanotechnology* **2020**, *31*, 205203/1−7.
(11) Lanza, M.; Zhang, K.; Porti, M.; Nafría, M.; Shen, Z. Y.; Liu, L. F.; Kang, J. F.; Gilmer, D.; Bersuker, G. Grain boundaries as preferential sites for resistive switching in the HfO_2 resistive random access memory structures. *Appl. Phys. Lett.* **2012**, *100*, 123508.
(12) Goh, Y.; Cho, S. H.; Park, S. H.; Jeon, S. Oxygen vacancy control as a strategy to achieve highly reliable hafnia ferroelectrics using oxide electrode. *Nanoscale* **2020**, *12*, 9024−9031.
(13) Mueller, M. P.; Pingen, K.; Hardtdegen, A.; Aussen, S.; Kindsmueller, A.; Hoffmann-Eifert, S.; De Souza, R. A. Cation diffusion in polycrystalline thin films of monoclinic HfO_2 deposited by atomic layer deposition. *APL Mater.* **2020**, *8*, 81104/1−8.
(14) Kim, S. B.; Ahn, Y. H.; Park, J. Y.; Lee, S. W. Enhanced nucleation and growth of HfO_2 thin films grown by atomic layer deposition on graphene. *J. Alloy. Compd.* **2018**, *742*, 676−682.
(15) Petzold, S.; Zintler, A.; Eilhardt, R.; Piros, E.; Kaiser, N.; Sharath, S. U.; Vogel, T.; Major, M.; McKenna, K. P.; Molina-Luna, L.; Alff, L. Forming-free grain boundary engineered hafnium oxide resistive random access memory devices. *Adv. Electron. Mater.* **2019**, *5*, 1900484/1−9.
(16) Hensling, F. V. E.; Keeble, D. J.; Zhu, J.; Brose, S.; Xu, C.; Gunkel, F.; Danylyuk, S.; Nonnenmann, S. S.; Egger, W.; Dittmann, R. UV radiation enhanced oxygen vacancy formation caused by the PLD plasma plume. *Sci. Rep.* **2018**, *8*, 8846.
(17) Zou, B.; Walker, C.; Wang, K.; Tileli, V.; Shaforost, O.; Harrison, N. M.; Klein, N.; Alford, N. M.; Petrov, P. K. Growth of epitaxial oxide thin films on graphene. *Sci. Rep.* **2016**, *6*, 31511.
(18) Kim, J.; Bayram, C.; Park, H.; Cheng, C. W.; Dimitrakopoulos, C.; Ott, J. A.; Reuter, K. B.; Bedell, S. W.; Sadana, D. K. Principle of direct van der Waals epitaxy of single-crystalline films on epitaxial graphene. *Nat. Commun.* **2014**, *5*, 4836/1−7.
(19) Tang, X.; Reckinger, N.; Poncelet, O.; Louette, P.; Urena, F.; Idrissi, H.; Turner, S.; Cabosart, D.; Colomer, J. F.; Raskin, J. P.; Hackens, B.; Francis, L. A. Damage evaluation in graphene underlying atomic layer deposition dielectrics. *Sci. Rep.* **2015**, *5*, 13523/1−12.
(20) Rodenbücher, C.; Hildebrandt, E.; Szot, K.; Sharath, S. U.; Kurian, J.; Komissinskiy, P.; Breuer, U.; Waser, R.; Alff, L. Hafnium carbide formation in oxygen deficient hafnium oxide thin films. *Appl. Phys. Lett.* **2016**, *108*, 252903.
(21) Weisenseel, B.; Harris, J.; Stumpf, M.; Wolf, S. E.; Fey, T.; Greil, P. Enhancement of the carbothermal reduction of hafnium oxide by silicon. *Adv. Eng. Mater.* **2017**, *19*, 1600377/1−9.
(22) Sabitova, A.; Ebert, Ph.; Lenz, A.; Schaafhausen, S.; Ivanova, L.; Daehne, M.; Hoffmann, A.; Dunin-Borkowski, R. E.; Foerster, A.; Grandidier, B.; Eisele, H. Intrinsic bandgap of cleaved ZnO(11-20) surfaces. *Appl. Phys. Lett.* **2013**, *102*, 21608/1−4.
(23) Ebert, Ph.; Schaafhausen, S.; Lenz, A.; Sabitova, A.; Ivanova, L.; Daehne, M.; Hong, Y. L.; Gwo, S.; Eisele, H. Direct measurement of the band gap and Fermi level position at InN(11-20). *Appl. Phys. Lett.* **2011**, *98*, 62103/1−3.
(24) Lee, J.; Sorescu, D. C.; Deng, X. Tunable lattice constant and band gap of single- and few-layer ZnO. *J. Phys. Chem. Lett.* **2016**, *7*, 1335−1340.
(25) Ugeda, M. M.; Bradley, A. J.; Shi, S. F.; da Jornada, F. H.; Zhang, Y.; Qiu, D. Y.; Ruan, W.; Mo, S. K.; Hussain, Z.; Shen, Z. X.; Wang, F.; Louie, S. G.; Crommie, M. F. Giant bandgap renormalization and excitonic effects in a monolayer transition metal dichalcogenide semiconductor. *Nat. Mater.* **2014**, *13*, 1091−1095.
(26) Lu, C. P.; Li, G.; Mao, J.; Wang, L. M.; Andrei, E. Y. Bandgap, mid-gap states, and gating effects in MoS_2. *Nano Lett.* **2014**, *14*, 4628−4633.
(27) Oganov, A. R.; Glass, C. W. Crystal structure prediction using ab initio evolutionary techniques: Principles and applications. *J. Chem. Phys.* **2006**, *124*, 244704/1−15.
(28) Oganov, A. R.; Ma, Y.; Lyakhov, A. O.; Valle, M.; Gatti, C. Evolutionary crystal structure prediction as a method for the discovery of minerals and materials. *Rev. Mineral. Geochem.* **2010**, *71*, 271−298.
(29) Oganov, A. R.; Lyakhov, A. O.; Valle, M. How evolutionary crystal structure prediction works and why. *Acc. Chem. Res.* **2011**, *44*, 227−237.
(30) Lyakhov, A. O.; Oganov, A. R.; Stokes, H. T.; Zhu, Q. New developments in evolutionary structure prediction algorithm USPEX. *Comput. Phys. Commun.* **2013**, *184*, 1172−1182.
(31) Kresse, G.; Hafner, J. Ab initio molecular dynamics for liquid metals. *Phys. Rev. B* **1993**, *47*, 558−561.
(32) Kresse, G.; Furthmüller, J. Efficient iterative schemes for ab initio total-energy calculations using plane-wave basis set. *Phys. Rev. B* **1996**, *54*, 11169−11186.
(33) Kresse, G.; Joubert, D. From ultrasoft pseudopotentials to the projector augmented-wave method. *Phys. Rev. B: Condens. Matter* **1999**, *59*, 1758−1775.
(34) Blöchl, P. E. Projector augmented-wave method. *Phys. Rev. B* **1994**, *50*, 17953−17979.
(35) Perdew, J. P.; Burke, K.; Ernzerhof, M. Generalized gradient approximation made simple. *Phys. Rev. Lett.* **1996**, *77*, 3865−3868.
(36) Krukau, A. V.; Vydrov, O. A.; Izmaylov, A. F.; Scuseria, G. E. Influence of the exchange screening parameter on the performance of screened hybrid functionals. *J. Chem. Phys.* **2006**, *125*, 224106−5.
(37) U.S. Dept. of Commerce Stull, D. R.; Prophet, H. *JANAF Thermochemical Tables*; National Bureau of Standards: Washington, D.C, 1971.

https://doi.org/10.1021/acsanm.2c04165
ACS Appl. Nano Mater. 2023, 6, 148−159

(38) Xu, C.; Wicklein, S.; Sambri, A.; Amoruso, S.; Moors, M.; Dittmann, R. Impact of the interplay between nonstoichiometry and kinetic energy of the plume species on the growth mode of SrTiO3 thin films. *J. Phys. D Appl. Phys.* **2014**, *47*, 34009/1−11.
(39) Zhao, X.; Vanderbilt, D. First-principles study of structural, vibrational, and lattice dielectric properties of hafnium oxide. *Phys. Rev. B: Condens. Matter* **2002**, *65*, 233106/1−4.
(40) Sang, X.; Grimley, E. D.; Schenk, T.; Schroeder, U.; LeBeau, J. M. On the structural origins of ferroelectricity in HfO_2 thin films. *Appl. Phys. Lett.* **2015**, *106*, 162905.
(41) Yate, L.; Coy, L. E.; Aperador, W. Robust tribo-mechanical and hot corrosion resistance of ultra-refractory Ta-Hf-C ternary alloy films. *Sci. Rep.* **2017**, *7*, 3080−9.
(42) Vargas, M.; Murphy, N. R.; Ramana, C. V. Structure and optical properties of nanocrystalline hafnium oxide thin films. *Opt. Mater.* **2014**, *37*, 621−628.
(43) Illarionov, Y. Yu.; Knobloch, T.; Jech, M.; Lanza, M.; Akinwande, D.; Vexler, M. I.; Mueller, T.; Lemme, M. C.; Fiori, G.; Schwierz, F.; Grasser, T. Insulators for 2D nanoelectronics: the gap to bridge. *Nat. Commun.* **2020**, *11*, 3385−15.
(44) Feenstra, R.; Stroscio, J. Tunneling spectroscopy of the GaAs(110) surface. *J. Vac. Sci. Technol. B* **1987**, *5*, 923−929.
(45) Chouprik, A.; Negrov, D.; Tsymbal, E. Y.; Zenkevich, A. Defects in ferroelectric HfO_2. *Nanoscale* **2021**, *13*, 11635−11678.
(46) McKenna, K.; Shluger, A. The interaction of oxygen vacancies with grain boundaries in monoclinic HfO(2). *Appl. Phys. Lett.* **2009**, *95*, 222111/1−3.
(47) Rushchanskii, K. Z.; Blügel, S.; Ležaić, M. Ordering of oxygen vacancies and related ferroelectric properties in $HfO_{2-\delta}$. *Phys. Rev. Lett.* **2021**, *127*, 087602.
(48) Funck, C.; Menzel, S. Comprehensive model of electron conduction in oxide-based memristive devices. *ACS Appl. Electron. Mater.* **2021**, *3*, 3674−3692.
(49) Krause, D.; Thornig, P. JURECA: Modular supercomputer at Jülich Supercomputing Centre. *JLSRF* **2018**, *4*, A132.
(50) Momma, K.; Izumi, F. VESTA 3 for three-dimensional visualization of crystal, volumetric and morphology data. *J. Appl. Crystallogr.* **2011**, *44*, 1272−1276.

https://doi.org/10.1021/acsanm.2c04165
ACS Appl. Nano Mater. 2023, 6, 148−159